Supplementary information

Interface-Enhanced $Ni_3S_2/LaNiO_3$ Heterostructure for Efficient Water Oxidation

Yana Liu,[a] Zidong He,[a] Yichao Hou,[a] Yizhen Ye,[a] Haodian Xie,[a] Wei Shen,[a] Pinxian Xi *[a] and Chun-Hua Yan [ab]

[a]State Key Laboratory of Natural Product Chemistry, Frontiers Science Center for Rare Isotopes, College of Chemistry and Chemical Engineering, Lanzhou University, Lanzhou 730000, China.

[b]Beijing National Laboratory for Molecular Sciences, State Key Laboratory of Rare Earth Materials Chemistry and Applications, PKU-HKU Joint Laboratory in Rare Earth Materials and Bioinorganic Chemistry, College of Chemistry and Molecular Engineering, Peking University, Beijing 100871, China.

*E-mail: xipx@lzu.edu.cn

Contents

1. Experimental Section

1.1 Materials

Lanthanum nitrate hexahydrate ($La(NO_3)_3 \cdot 6H_2O$, 99.99%), nickel nitrate hexahydrate ($Ni(NO_3)_2 \cdot 6H_2O$, 98%), 1,3,5-Benzenetricarboxylic acid (1,3,5-BTC, 99.0%), N,N-dimethylacetamide (DMAC, 99.8%), thiourea (NH_2CSNH_2, 99%), anhydrous ethanol (EtOH, 99.5%), potassium hydroxide (KOH, 99.9%) were purchased from Aladdin. All the experimental water was ultra-pure water (Millipore milliq grade) with a resistivity of ~18.25 megohms. All the other materials for electrochemical measurements were analytical grade and can be used without further purification.

The commercial carbon cloth was purchased from Fuel Cell Store. To enhance the hydrophilicity of the carbon cloth for achieving uniform loading of self-supporting materials and improving its mechanical stability, the purchased carbon cloth was subjected to an activation pretreatment. First, the carbon cloth cut into 2 cm * 2 cm pieces was ultrasonically cleaned with acetone and ethanol for 15 minutes each to remove residual oil stains on the surface from mechanical processing. Then, an appropriate amount of nitric acid was added just enough to cover the carbon cloth for activation treatment. After that, it was rinsed thoroughly with plenty of deionized water. Finally, alternating ultrasonic cleaning with deionized water and ethanol was performed for 15 minutes each cycle, repeated 2-3 times. The activated carbon cloth was stored in deionized water for later use.

1.2 Materials Synthesis

Synthesis of $LaNiO_3$: The stoichiometric $La(NO_3)_3 \cdot 6H_2O$ (0.5 mmol) and $Ni(NO_3)_2 \cdot 6H_2O$ (0.5 mmol) were dissolved in DMAC (60 mL) and stirred for 10 min to form a clarified solution. Then, 1,3,5-BTC (1.2 mmol) was added to the above solution and stirred for 1 h. The solution was transferred to a 100 mL Teflon-lined stainless-steel autoclave, kept at 130 °C for 10 h, centrifuged at 7000 rpm for 5 min, and washed five times with anhydrous ethanol. The product was dried at 60 °C for 3 h and annealed at 650 °C (1 °C min^{-1}) for 5 h to obtain $LaNiO_3$.

Synthesis of LNO-TU: LNO was dispersed in a mixed solution of isopropanol and water (volume ratio 1:3) to obtain a dispersion with a concentration of 2 mg/mL. An appropriate amount of the dispersion was loaded onto carbon cloth with a loading mass of 0.2 mg cm^{-2}. Cyclic voltammetry (CV) electrodeposition was then performed in a 1 mol/L thiourea solution, using a Pt plate as the counter electrode and Ag/AgCl as the reference electrode. The CV window was set at −1.2 to 0.2 V (*vs*. Ag/AgCl) with a scan rate of 5 mV/s. After 20 cycles of deposition, LNO-TU was obtained.

Synthesis of Ni_3S_2: Using the same electrodeposition conditions as described for LNO-TU, clean carbon cloth was subjected to CV electrodeposition in a solution containing 1 M thiourea and 0.1 M Ni^{2+}. By varying the number of CV cycles, three samples were prepared: Ni_3S_2-I (10 cycles), Ni_3S_2-II (20 cycles), and Ni_3S_2-III (30 cycles).

Synthesis of Ni_3S_2/LNO: The procedure was similar to that of LNO-TU, except that the electrodeposition solution was replaced with one containing 1 M thiourea and 0.1 M Ni^{2+}. By controlling the number of CV deposition cycles, three samples were obtained: Ni_3S_2/LNO-I (10 cycles), Ni_3S_2/LNO-II (20 cycles), and Ni_3S_2/LNO-III (30 cycles).

1.3 Materials Characterizations

XRD measurements were made on Rigaku MiniFlex 600 diffractometer at 40 kV and under Cu

Kα radiation in the range of 10 to 90° (λ = 0.1542 nm). SEM and energy spectrum images were taken with Thermo Fisher Apreo S field emission scanning electron microscope (FE-SEM) at 30 kV acceleration voltage. TEM and HRTEM images were obtained by Tecnai G2 F30 field emission transmission electron microscopy. XPS analysis was performed with a Kratos Axis Supra unit and correction was performed with a C 1*s* line at 284.8 eV. The composition of the sample was determined by ICP-OES using plasma quantitative PQ9000 ICP spectrometer. Raman spectroscopy was measured on the LabRAM HR Evolution spectrophotometer and the excitation light source wavelength was 473 nm. BRUKER-Fourier Transform Infrared Spectrometer-TENSOR27 was used. The EQCM measurements were recorded using Gamry Instruments eQCM 15 M resonator and Gamry software.

1.4 Electrochemical Measurements

Electrochemical tests were performed at room temperature at the CHI-760E Electrochemical Workstation (CHI Instruments, Shanghai Chenhua Instrument Corp, China) in 1.0 M KOH solution using a standard three-electrode setup. Saturated Hg/HgO and Pt were used as reference electrode and counter electrode, respectively. The measured potential was converted to a reversible hydrogen electrode (RHE) by Nernst equation ($E_{RHE} = E_{Hg/HgO} + 0.0591pH + 0.098$, $E_{RHE} = E_{Ag/AgCl} + 0.0591pH + 0.197$). The electrolyte was purified with O_2 for 30 minutes before each measurement. CV measurements were performed at a scan rate of 5 mV s^{-1} in 1.0 M KOH. EIS measurements were made in the frequency range from 0.01 Hz to 100 kHz. Stability was performed by a chronopotentiometry test at the constant current densities of 10 and 100 mA cm^{-2} in 1.0 M KOH electrolyte. Double-layer capacitance (C_{dl}) was determined to estimate the electrochemically active surface area (ECSA) of the catalyst in 1 M KOH. Specifically, voltammetric measurements were performed within the non-Faradaic potential region at different scan rates. At each vertex potential, the working electrode was held for 30 s prior to initiating the subsequent sweep to ensure surface stabilization. In-situ attenuated total reflection infrared (ATR-IR) spectra were studied using saturated Ag/AgCl reference electrode and Pt counter electrode in 1.0 M KOH.

1.5 EQCM measurements

In-situ EQCM during the synthesis process. Taking the preparation of Ni_3S_2/LNO as an example, a 5 MHz gold-coated quartz crystal was used as the mass sensor. LNO was uniformly loaded onto the crystal surface as the working electrode, with a Pt wire as the counter electrode and an Ag/AgCl electrode as the reference electrode. CV electrodeposition was performed in an aqueous solution containing 1 M thiourea and 0.1 M $Ni(NO_3)_2$, with a potential window of -1.2 - 0.2 V (*vs*. Ag/AgCl) at a scan rate of 5 mV/s. The change in crystal frequency was recorded synchronously to calculate the mass change over 20 CV cycles.

In-situ EQCM during the catalytic process. The catalyst was uniformly dispersed in a mixed solvent (4 mg catalyst + 0.4 mL isopropanol + 1.6 mL ultrapure water + 20 μL Nafion solution). An aliquot containing 80 μg of catalyst was drop-cast onto the quartz crystal surface as the working electrode, with a Pt wire and an Ag/AgCl electrode serving as the counter and reference electrodes, respectively. In 1.0 M KOH, CV scans were performed at a scan rate of 5 mV/s within a potential window of 0.2 to 0.8 V (*vs*. Ag/AgCl) for 10 cycles, while the mass change was recorded synchronously. This provided insight into the mass evolution of the catalyst during the electrochemical reconstruction process. The change in mass per unit area (Δm) is calculated from

the change in resonance frequency (Δ*f*), using the Sauerbrey equation:

$$\Delta f = -\frac{2{f_0}^2}{A\sqrt{\mu_Q \rho_Q}}\Delta m$$

where f_0 is the resonant frequency of the quartz resonator, *A* is the area of the EQCM electrode, μ_Q is the shear modulus of the quartz, and ρ_Q is the density of the quartz.[1]

1.6 In-situ Raman

In-situ Raman spectroscopy during the synthesis process. Taking the preparation of Ni_3S_2/LNO as an example, a customized electrochemical cell was employed, using a Pt wire as the counter electrode, an Ag/AgCl electrode as the reference electrode, and LNO-loaded carbon cloth as the working electrode. CV electrodeposition was performed in an aqueous solution containing 1 M thiourea and 0.1 M $Ni(NO_3)_2$, with a potential window of -1.2 - 0.2 V (*vs*. Ag/AgCl) at a scan rate of 5 mV/s. A total of 20 CV cycles were conducted, and a Raman spectrum was collected after each cycle. The same procedure was applied to the control samples Ni_3S_2 (deposited directly onto clean carbon cloth) and LNO-TU (prepared in the absence of Ni^{2+} in the electrolyte).

In-situ Raman spectroscopy during the catalytic process. A customized electrochemical cell was used, with a Pt wire as the counter electrode, an Ag/AgCl electrode as the reference electrode, and catalyst-loaded carbon cloth as the working electrode. In 1 M KOH solution, a potentiostatic method was applied to step the potential to different values (corresponding to the potentials shown in Figs. 4b-c). After stabilization for 5 minutes at each potential, Raman spectra were collected.

2. Supplementary Figures

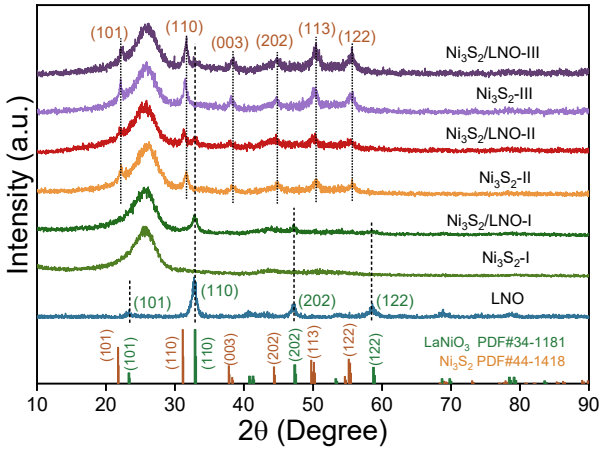

Figure S1. XRD patterns of samples.

The diffraction peaks of LNO are consistent with the standard card of perovskite-phase $LaNiO_3$ (PDF#34-1181), and the Miller indices of the main peaks (e.g., (101), (110)) are labeled in the figure. The diffraction peaks of Ni_3S_2 match the standard card of hexagonal-phase Ni_3S_2 (PDF#44-1418), and its characteristic peaks (e.g., (101), (110), (113)) are also labeled. The patterns of the Ni_3S_2/LNO composites contain characteristic peaks from both phases, confirming the successful construction of the heterostructure. Moreover, as the thickness of the Ni_3S_2 layer increases, the intensity of the LNO diffraction peaks gradually decreases, indicating successful coating of Ni_3S_2 on the LNO surface. Notably, the Ni_3S_2/LNO-I sample obtained after 10 CV electrodeposition cycles does not show obvious Ni_3S_2 diffraction peaks, suggesting that no well-defined crystalline structure has formed at this stage. In contrast, the Ni_3S_2/LNO-III sample obtained after 30 CV electrodeposition cycles exhibits an overly thick Ni_3S_2 layer, making it difficult to accurately detect the LNO signals. The Ni_3S_2/LNO-II sample obtained after 20 CV electrodeposition cycles clearly shows diffraction peaks corresponding to both LNO and Ni_3S_2. Therefore, to construct a well-defined oxide-sulfide heterostructure and fully exploit the respective advantages of LNO and Ni_3S_2, we selected Ni_3S_2/LNO-II for subsequent studies. Unless otherwise specified, Ni_3S_2/LNO in this work refers to Ni_3S_2/LNO-II, and Ni_3S_2 refers to Ni_3S_2-II.

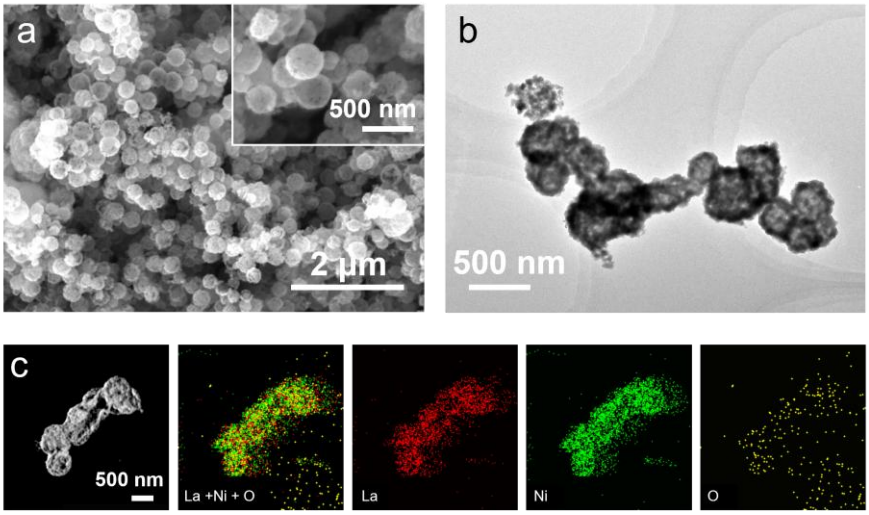

Figure S2. $LaNiO_3$: (a) SEM image, (b) TEM image, (c) Elemental mapping images.

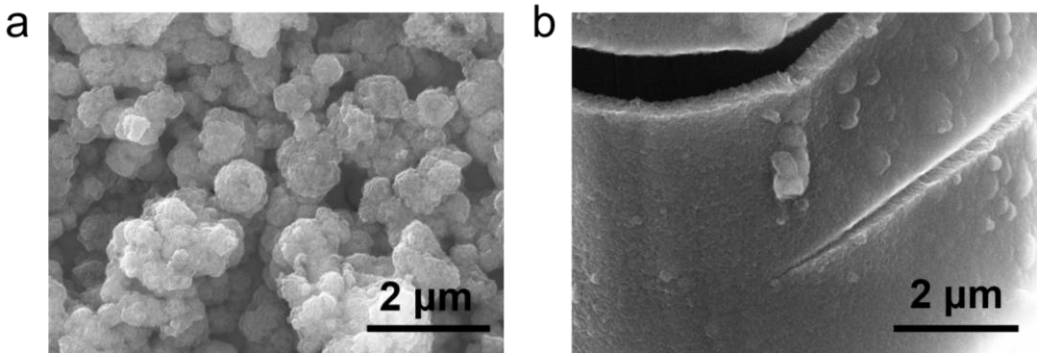

Figure S3. SEM images of (a) Ni_3S_2/LNO and (b) Ni_3S_2.

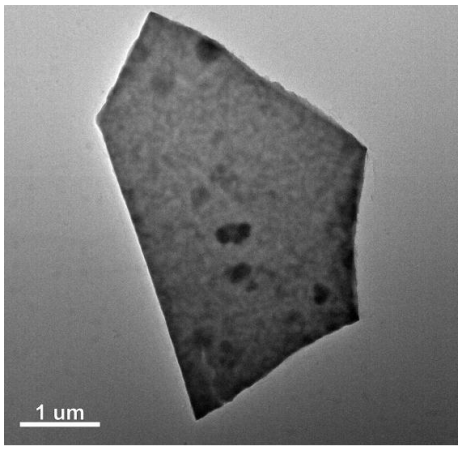

Figure S4. TEM image of Ni_3S_2.

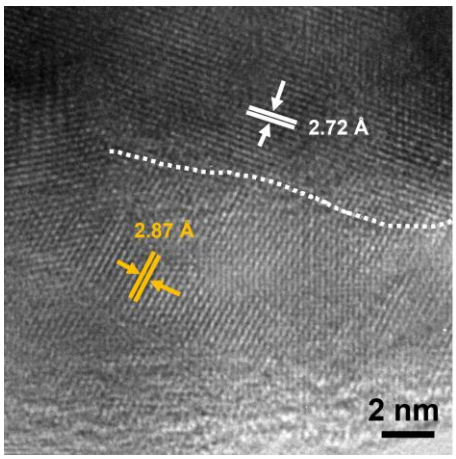

Figure S5. HRTEM image of Ni_3S_2/LNO.

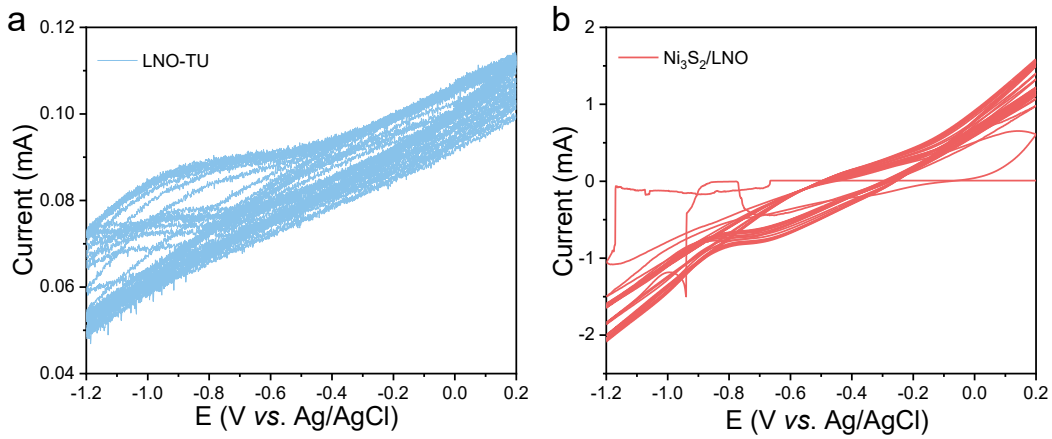

Figure S6. The electrochemical processes corresponding to the EQCM measurements during electrodeposition.

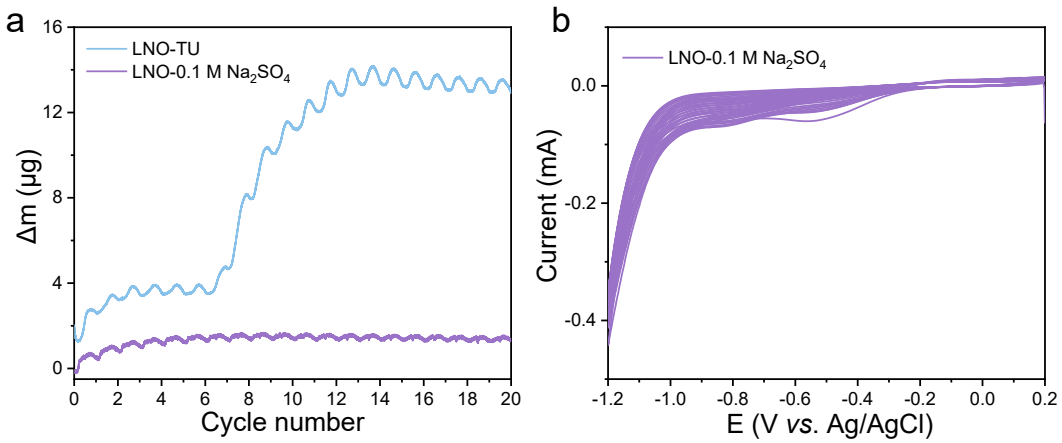

Figure S7. (a) EQCM response of LNO in thiourea aqueous solution and 0.1M Na_2SO_4 solution. (b) The electrochemical processes corresponding to the EQCM measurement during electrodeposition of LNO in 0.1M Na_2SO_4 solution.

The results showed that LNO exhibited only a very weak mass change in Na_2SO_4, which was significantly smaller than the mass increase observed in the thiourea-containing solution. This comparison clearly indicates that the mass increase of LNO in the thiourea solution mainly originates from the O-S exchange process.

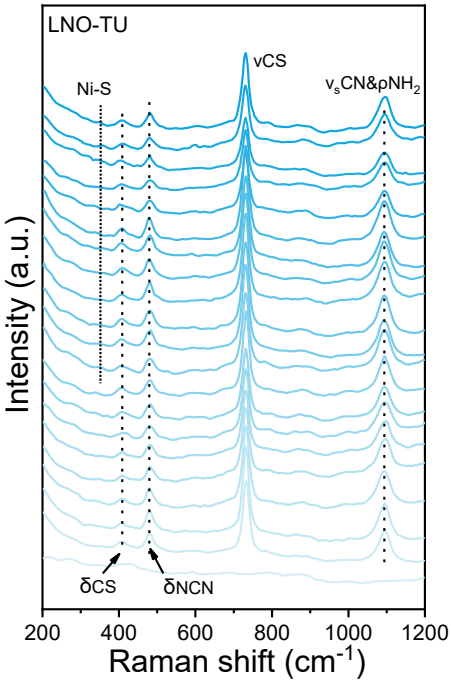

Figure S8. The in-situ Raman spectra collected during the process of preparing LNO-TU by electrodeposition.

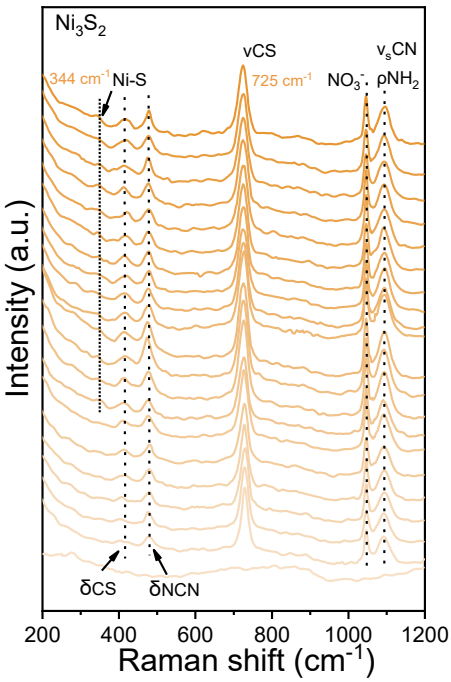

Figure S9. The in-situ Raman spectra collected during the process of preparing Ni_3S_2 by electrodeposition.

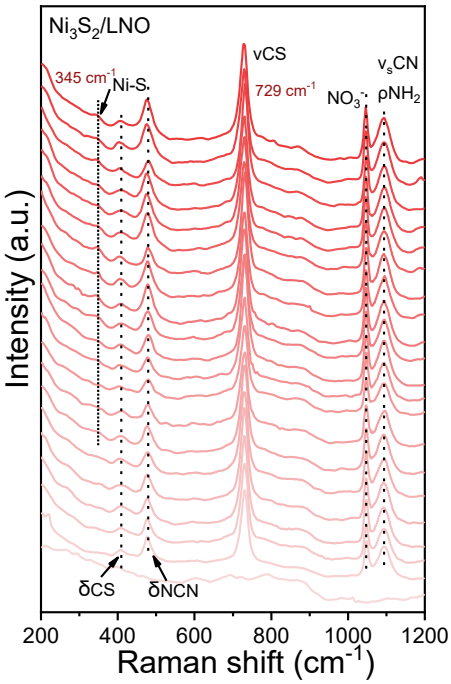

Figure S10. The in-situ Raman spectra collected during the process of preparing Ni_3S_2/LNO by electrodeposition.

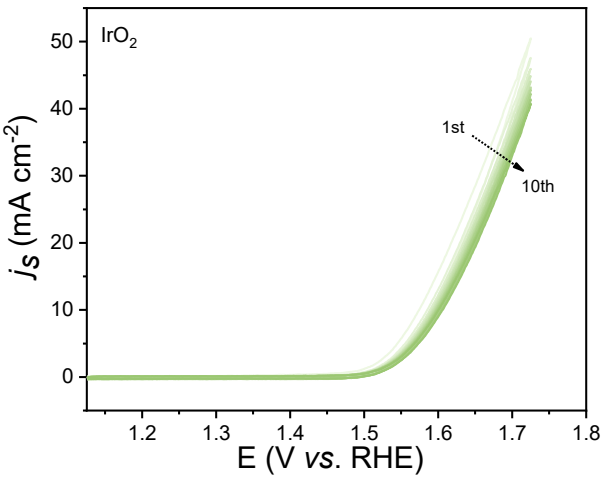

Figure S11. Multiple CV cycles of commercial IrO_2.

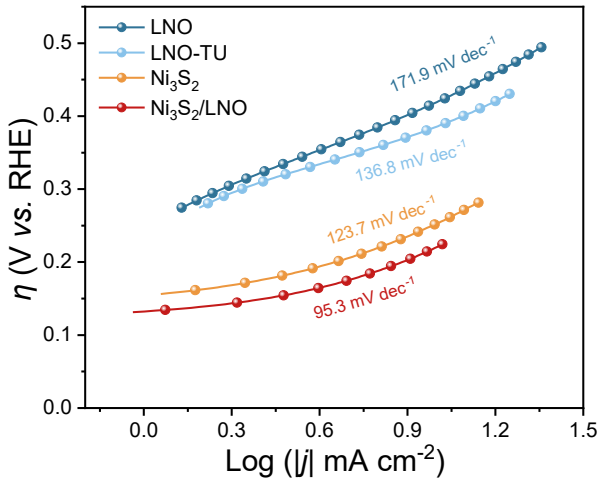

Figure S12. Tafel plots of as-synthesized LNO, LNO-TU, Ni_3S_2, and Ni_3S_2/LNO.

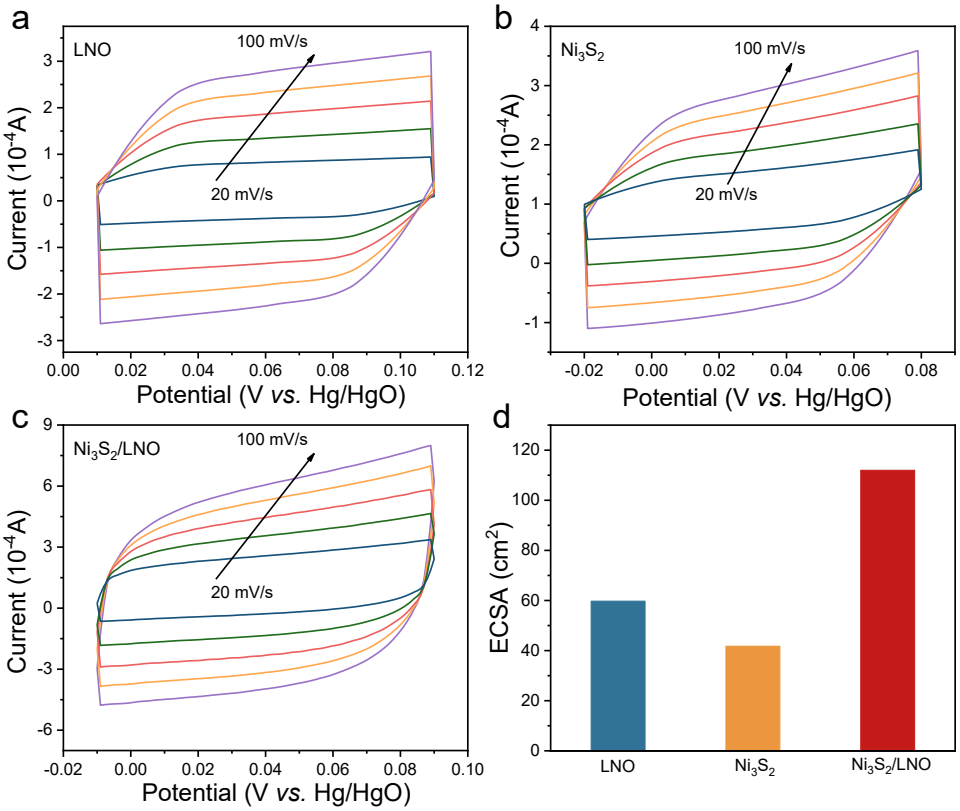

Figure S13.DLC tests for (a) LNO, (b) Ni_3S_2, and (c) Ni_3S_2/LNO. (d) ECSA of those materials.

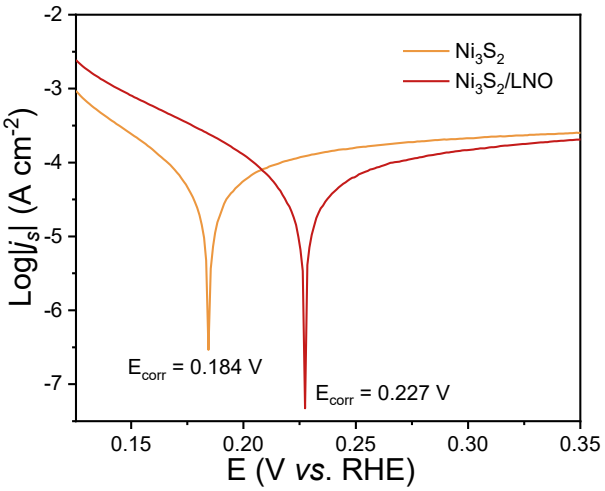

Figure S14. Corrosion polarization curves of Ni_3S_2 and Ni_3S_2/LNO.

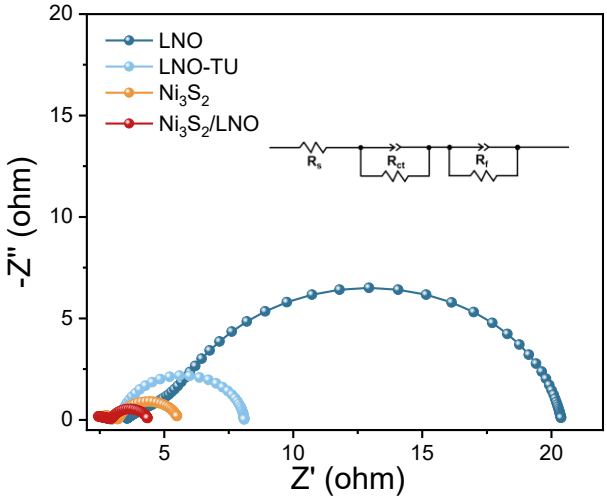

Figure S15. Nyquist plots of LNO, LNO-TU, Ni_3S_2, and Ni_3S_2/LNO.

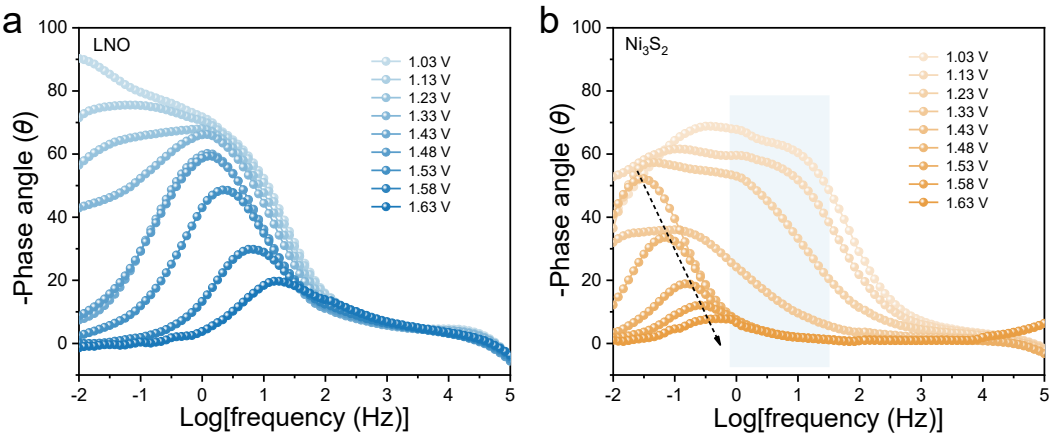

Figure S16. Bode plots of (a) pure LNO and (b) Ni_3S_2 at different applied potentials *vs*. RHE in 1 M KOH. The mid-frequency peak is associated with surface double-layer capacitance, where a larger value indicates stronger OH^- affinity and more favorable reaction kinetics.

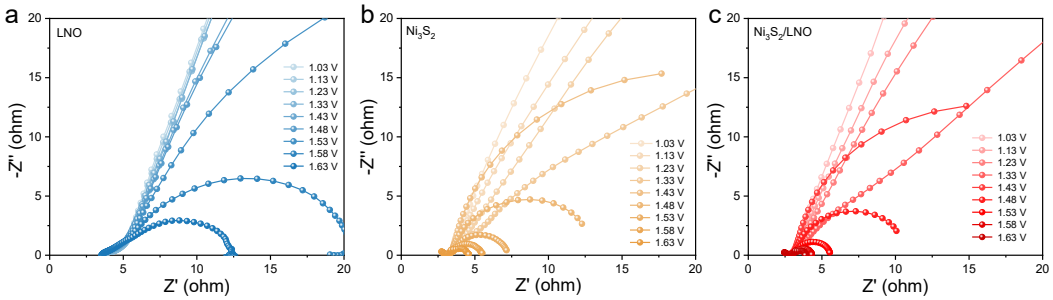

Figure S17. Nyquist plots of (a) LNO, (b) Ni_3S_2, and (c) Ni_3S_2/LNO at increasing applied potentials from 1.03 V to 1.63 V (*vs*. RHE).

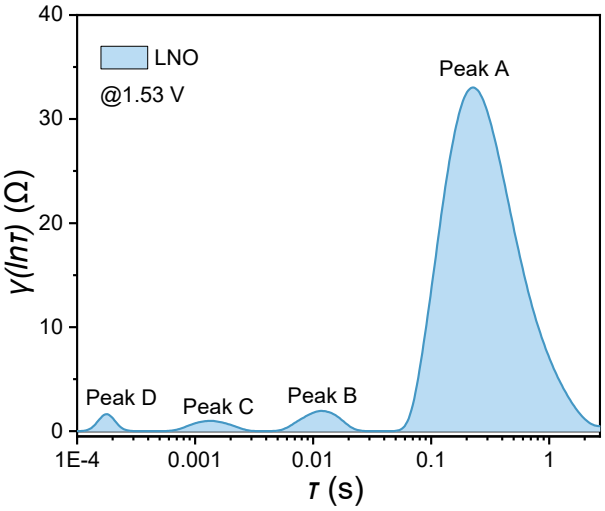

Figure S18. DRT of LNO at 1.53 V (*vs*. RHE).

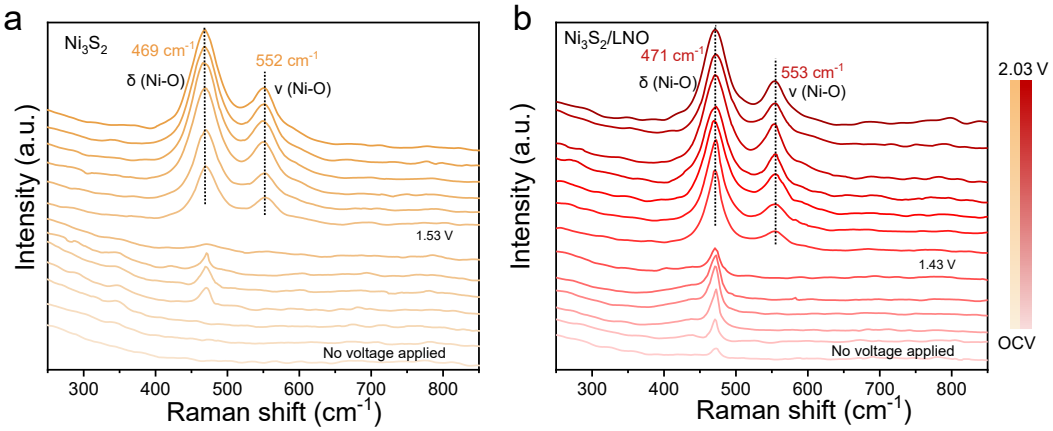

Figure S19. In-situ Raman spectra of (a) Ni_3S_2 and (b) Ni_3S_2 /LNO. Raman bands at ~469 cm^{-1}, and ~552 cm^{-1} are assigned to Ni-O bending vibration and Ni-O stretching vibration, respectively.[2]

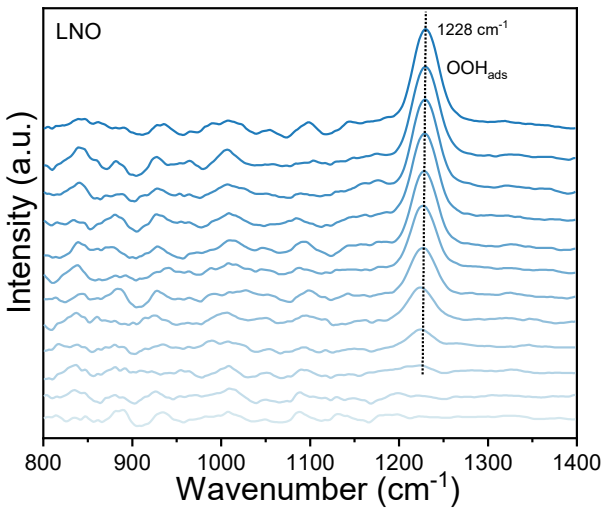

Figure S20. In-situ ATR-IR spectra recorded during the multi-potential steps for LNO.

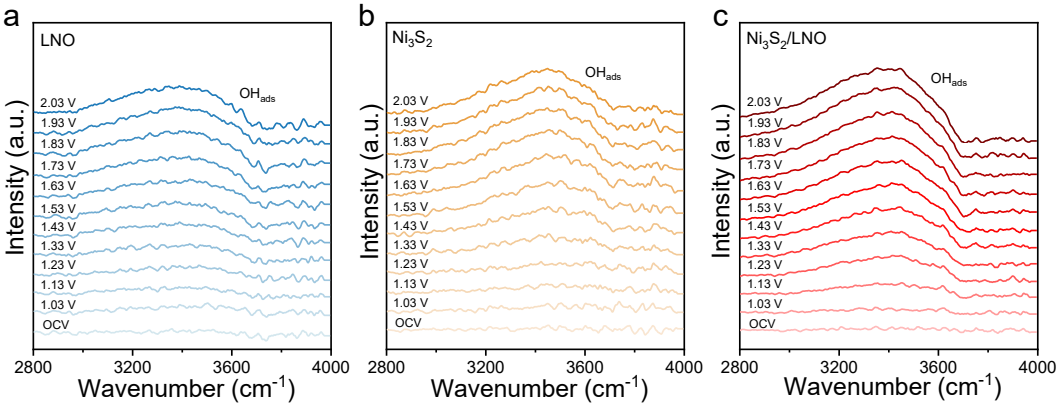

Figure S21. In-situ ATR-IR spectra recorded during the multi-potential steps for (a) LNO, (b) Ni_3S_2, and (c) Ni_3S_2/LNO.

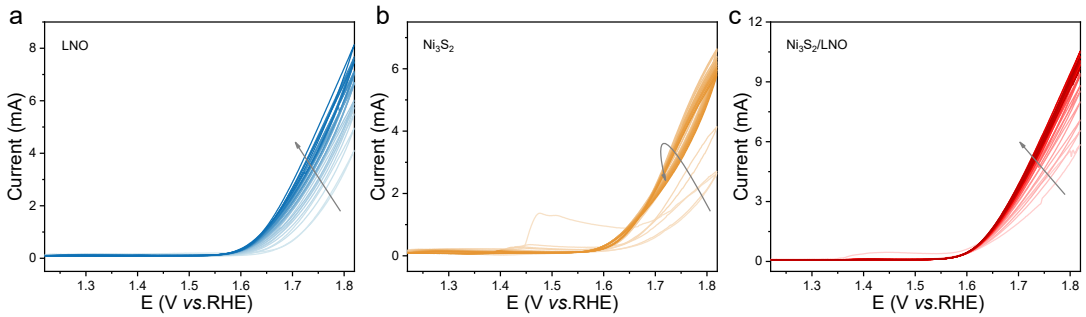

Figure S22. The corresponding CV data during the EQCM analysis of (a) LNO, (b) Ni_3S_2, and (c) Ni_3S_2/LNO.

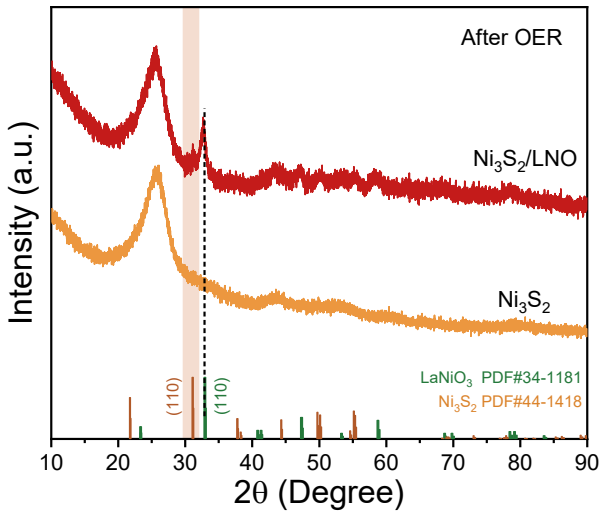

Figure S23. XRD patterns of Ni_3S_2 and Ni_3S_2/LNO after OER tests. For Ni_3S_2, the characteristic diffraction peaks disappear after the test, indicating the occurrence of severe overoxidation. In contrast, for the Ni_3S_2/LNO heterostructure, the characteristic peak corresponding to the (110) plane of Ni_3S_2 remains visible, suggesting that the presence of LNO effectively suppresses the excessive oxidation of Ni_3S_2 under oxidizing potentials.

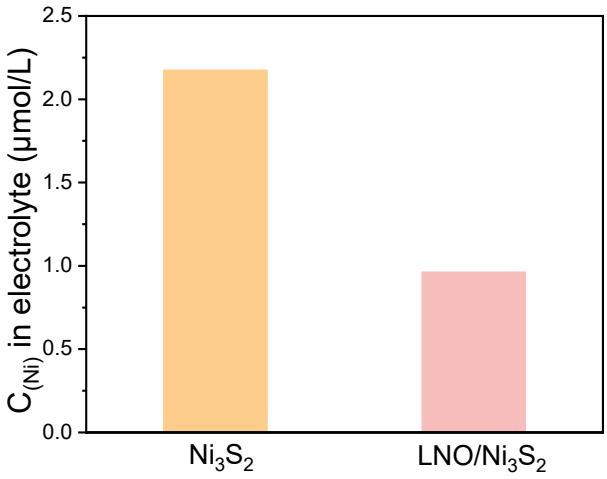

Figure S24. The Ni ion concentration in the electrolyte corresponding to the both catalysts measured by ICP-OES after OER tests.

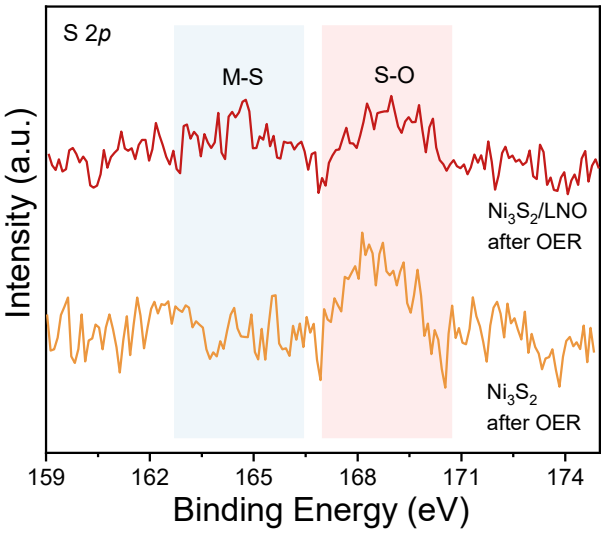

Figure S25. S 2*p* XPS spectra of Ni_3S_2 and Ni_3S_2/LNO after OER test.

3. Supplementary Tables

Table S1. The OER performance of Ni_3S_2/LNO compared with recently reported catalysts.

Catalysts	Overpotentials	Stability	Electrolyte	References
$NiCo_2O_4$-HNF	236 mV/10 m A cm^{-2}	30 h/100 mA cm^{-2}	1 M KOH	3
$Ba_{0.3}Sr_{0.7}CoO_{3-\delta}$-h	236 mV/10 m A cm^{-2}	AEMWE	1 M KOH	4
Fe/$NiPS_3$-4	242 mV/10 m A cm^{-2}	AEMWE	1 M KOH	5
RuO_x/γ-MnO_2	255 mV/10 m A cm^{-2}	300 h/10 mA cm^{-2}	1 M KOH	6
$LaNiO_3/Fe_2O_3$-Co	273 mV/10 m A cm^{-2}	18 h/280 mV	1 M KOH	7
$LNFe^{III}$-*spe*	280 mV/10 m A cm^{-2}	300 h/10 mA cm^{-2}	1 M KOH	8
Fe–Ni_3S_4/Cr_2O_3	282 mV/10 m A cm^{-2}	100 h/10 mA cm^{-2}	1 M KOH	9
g-$NiOOH_{Mo\text{-}SR}$/NF	302 mV/10 m A cm^{-2}	AEMWE	1 M KOH	10
$Co_{0.7-x}Fe_{0.3-y}P/Co_xFe_yOOH$	256 mV/10 m A cm^{-2}	80 h/100 mA cm^{-2}	1 M KOH	11
$NiCo_2O_4$-F_1	300 mV/10 m A cm^{-2}	36 h/100 mA cm^{-2}	1 M KOH	12
$Pr_{0.75}Sr_{0.25}Ni_{0.7}Co_{0.3}O_3$	389 mV/10 m A cm^{-2}	120 h/10 mA cm^{-2}	1 M KOH	13
Ni_3S_2/LNO	221 mV/10 m A cm^{-2}	500 h/100 mA cm^{-2}	1 M KOH	This work

4. References

1 D. A. Buttr and M. D. Ward, *Chem. Rev.*, 1992, **92**, 1355-1379.
2 S. Qi, J. You, X. Liufu, Y. Zhang, R. Chen, J. Zhuang, T. Liang, L. Li, Q. Huo, C. Shang, X. Zhang, H. Yang, Q. Hu and C. He, *Adv. Mater.*, 2026, **38**, e12188.
3 T. Li, W. Shi, J. Meng, Y.-Q. Liu, H. Zhao, Y. Wang and X. Shao, *ACS Catal.*, 2026, **16**, 4855-4867.
4 Q. Zhang, H. Zhong, C. Wu, J. Yu, Z. G. Yu, C. Diao, X. Li, Y. Hua, S. Xi, X. Wang and J. Xue, *ACS Nano*, 2025, **19**, 39480-39490.
5 Y. Liu, L. Li, X. Li, Y. Xu, D. Wu, T. Sakthivel, Z. Guo, X. Zhao and Z. Dai, *Sci. Adv.*, 2025, **11**, eads0861.
6 T. Pan, W. H. Huang, H. Jie, M. H. Yeh, K. Li, M. Chen, X. Zhou, J. Ge, X. Li, X. Zhao, Z. Hu, Y. Liu, J. Ma and H. Cheng, *Adv. Funct. Mater.*, 2025, **36**, e17063.
7 C. Ye, Z. Yu, J. Yang, J. Xie, Y. Huang, J. Gao, G. Xu, J. Xu, Z. Pan, Y. Liu, L. Liu, X. Wang and Z. Tai, *Angew. Chem., Int. Ed.*, 2025, **64**, e202422451.
8 J. W. Zhao, K. Yue, L. Wu, J. Yang, D. Luan, X. Zhang and X. W. Lou, *Angew. Chem., Int. Ed.*, 2025, **64**, e202507144.
9 K. Wang, C. Ni, L. Jin, X. Qian, H. Xu, H. Chen and G. He, *Chem. Sci.*, 2025, **16**, 7467-7476.
10 H. Zhi, Z. Liao, H. Jiang, Y. He, Z. Chen, S. Yang and H. Zhang, *Chem. Commun.*, 2026, **62**, 289-292.
11 J. Fan, J. Jiang, Y. Wang, X. Zhang, Y. Liu, X. Yang, T. Pan, D. Xu, N. Shi, Y. Lin, M. Han and H. Pang, *Adv. Funct. Mater.*, 2025, **35**, 2425770.
12 Y. Yue, X. Zhong, M. Sun, J. Du, W. Gao, W. Hu, C. Zhao, J. Li, B. Huang, Z. Li and C. Li, *Adv. Mater.*, 2025, **37**, 2418058.
13 S. Ma, X. Li, T. Liu, K. Yuan, M. Tang, W. Muhammad, X. He, T. Ouyang, X. Zhang, W. Tao, Y. Niu, Z. Zhang and W. Lv, *Small Methods*, 2026, **10**, e02223.